PCCP

PAPER

View Article Online
View Journal | View Issue

Cite this: *Phys. Chem. Chem. Phys.*, 2017, **19**, 22546

Stability of dye-sensitized solar cells under extended thermal stress†

Surendra K. Yadav,[a] Sandheep Ravishankar,[b] Sara Pescetelli,[a] Antonio Agresti,[a] Francisco Fabregat-Santiago*[b] and Aldo Di Carlo*[a]

Received 8th July 2017,
Accepted 28th July 2017

DOI: 10.1039/c7cp04598k

rsc.li/pccp

In the last few decades, dye-sensitized solar cell (DSC) technology has been demonstrated to be a promising candidate for low cost energy production due to cost-effective materials and fabrication processes. Arguably, DSC stability is the biggest challenge for making this technology appealing for industrial exploitation. This work provides further insight into the stability of DSCs by considering specific dye–electrolyte systems characterized by Raman and impedance spectroscopy analysis. In particular, two ruthenium-based dyes, Z907 and Ru505, and two commercially available electrolytes, namely, the high stability electrolyte (HSE) and solvent-free Livion 12 (L-12), were tested. After 4700 h of thermal stress at 85 °C, the least stable device composed of Z907/HSE showed an efficiency degradation rate of ~14%/1000 h, while the Ru505/L-12 system retained 96% of its initial efficiency by losing ~1% each 1000 h. The present results show a viable route to stabilize the DSC technology under prolonged annealing conditions complying with the IEC standard requirements.

Introduction

The stability of DSCs[1] is an important aspect to be addressed prior to their commercialization. However, the evaluation of the solar cell lifetime is a difficult task since it depends on the specific degradation mechanisms[2] involving chemical/physical modifications of constituent materials and interfaces (intrinsic degradations) as well as structural module failure (extrinsic degradations). Therefore, with the aim to address the DSC stability issue, the understanding of intrinsic/extrinsic degradation mechanisms permits the designing of stable and high performing materials as well as to help optimize fabrication processes. In this context, several studies have already evaluated the intrinsic deterioration under different kinds of aging tests such as reverse bias,[3–5] thermal stress,[6] temperature cycles,[7] light soaking[8] and outdoor conditions.[9] Some of these harsh stress conditions may be prevented by an adequate protection strategy; for example, reverse bias degradation may be avoided by an effective diode protection strategy retaining low voltages across the reverse biased cells. However, under real working conditions, DSCs can undergo severe unavoidable thermal stress (operating temperature up to 80 °C), inducing permanent electrolyte degradation and eventually, loss of photovoltaic performance. As a matter of fact, the use of volatile solvents in the electrolyte solution together with non-robust sealing frequently results in solvent chemical instability and electrolyte solution leakage with a consequent chemical degradation of the device photo-electrode (PE) until complete device breakdown.[10]

For these reasons, sealing should be hermitic to prevent moisture entrance and at the same time flexible enough to endure thermal expansion of the cell's constituent elements[11–13] under real working conditions.

Among the several works reporting on DSCs thermal stability, R. Harikisun *et al.*[14] extrapolated DSC lifetimes of 40 years and 25 years for Central European and Southern European conditions, respectively, by means of accelerated ageing tests. In particular, 80 °C storage over 1000 h resulted in 10–20% decrease of performance with ionic liquid or solvent-based electrolyte systems. Similarly, T. Stergiopoulos *et al.*[15] obtained a long-term stability of about 5000 h when non-nitrile solvents are employed in the electrolyte solution. In particular, 3000 h light soaking exposure followed by 2000 h at 85 °C induced a power conversion efficiency (PCE) reduction of only 10% in the case of a tetraglyme-based electrolyte.[15,16] Moreover, W. Yang and co-workers recently reported DSCs employing a novel cobalt bipyridyl-based electrolyte that passed a 1200 h at 70 °C test by retaining 80% of its initial open circuit voltage (V_{oc}).[6]

[a] *C.H.O.S.E. (Centre for Hybrid and Organic Solar Energy), Department of Electronic Engineering, University of Rome "Tor Vergata", via del Politecnico 1, Rome, 00133, Italy. E-mail: aldo.dicarlo@uniroma2.it; Fax: +39-06-72597939; Tel: +390672597456*

[b] *Group of Advanced Materials and Energy, Institute of Advanced Materials (INAM), Universitat Jaume I, Castello de la Plana, 12006, Spain. E-mail: fabresan@uji.es; Tel: +34-964-387537*

† Electronic supplementary information (ESI) available: The UV-vis spectra and chemical structures of Z907 and Ru505 dyes (Fig. S1), electrical parameter trend under 85 °C thermal stress (Fig. S2), Nyquist spectra of Z907/L-12 samples at −0.62 V (Fig. S3), plot of recombination resistances *versus* equivalent conduction band for Z907 samples (Fig. S4), and IS analysis for Ru-505 based devices (Fig. S5). See DOI: 10.1039/c7cp04598k

In this work, thermal degradation mechanisms are investigated in DSCs employing two different ruthenium based dyes, namely (*cis*-RuLL′ $(SCN)_2$ (L = 4,4′-dicarboxylic acid-2,2′-bipyridine, L′ = 4,4′-dinonyl-2,2′-bipyridine)) Z907 and (*cis*-dicyano-bis(2,2-bipyridyl 4,4-dicarboxylic acid) ruthenium(II)) Ru505, combined with two different commercially available electrolytes having different viscosity properties, namely a high stability electrolyte (HSE, Dyesol) based on the 3-methoxypropionitrile – MPN – solvent and Livion 12 (L-12, Merck) as a solvent-free electrolyte (1-methyl-3-propylimidazolium iodide – PMIM-I + 1-ethyl-3-methylimidazolium tetracyanoborate – EMIM-TCB – in a volume ratio of 65/35).

The most popular inorganic sensitizers are the Ru(II) polypyridyl dyes. The success of this dye class is due to their excellent performance resulting from their broad light absorption range (from ultraviolet to near-infrared light), high molecular stability,[17] and their suitable energy levels matching with both TiO_2 photoanodes and iodine based electrolytes. Moreover, the chemical structure of the Ru(II) polypyridine molecules ensures a very efficient electron injection process to the TiO_2 (usually in the picosecond regime) through the carboxyl group and/or amino group (–COOH or $–NH_2$). On the other hand, the dye regeneration process is ensured through the ancillary ligands that strongly impact on the dye molecule stability under operative conditions.[18,19] In particular, the dye molecules Ru505 and Z907 differ mainly in the ancillary ligands, cyanide and thiocyanate, respectively.

Regarding the electrolytes, the I^-/I_3^- redox couple showed a higher PCE value[20] when coupled with Ru-based dyes. Moreover, the iodine-based redox couple ensures a high electrical conductivity that should be coupled to a low viscosity for faster diffusion of electrons within the working device. For these reasons, we selected two commercial iodine-based electrolytes with optimized formulation in terms of electrical conductivity and chemical stability but with different viscosities and boiling points. In this work, the four investigated device typologies are indicated on the basis of the employed dye/electrolyte couple as follows: Z907/HSE, Z907/L-12, Ru505/HSE and Ru505/L-12. In particular, Raman and impedance spectroscopies (RS and IS) were used for the determination of the dye/electrolyte couple that is able to pass prolonged thermal stress at 85 °C, complying with the IEC test protocols.

Experimental section

A fluorine-doped tin oxide (FTO, NSG TEC 8 $\Omega\ \square^{-1}$) conducting glass was firstly washed with acetone, then with ethanol and isopropanol according to the cleaning protocol. The mesoporous transparent film of TiO_2 (transparent TiO_2 paste DSL 18NR-T, Dyesol) was deposited onto the pre-cleaned FTO glass plate using a screen printing technique. The TiO_2 film was dried at ~80 °C for 20 min and then fired at 450 °C for ~30 min to remove organic materials and to form a crystalline TiO_2 mesoporous film structure. The TiO_2 electrode was gradually sintered in a furnace under an airflow with a temperature ramp rate of 15 °C min^{-1}. The final thickness of the TiO_2 film after sintering was 7 μm as measured using a profilometer (Dektak 150, Veeco). When the temperature was cooled down to 80 °C, the TiO_2 electrodes were dipped into Z907 or Ru505 dye solutions in ethanol and isopropanol respectively for 16 h in the dark to adsorb the dye onto the TiO_2 surface. The counter electrode (CE) was prepared by screen-printing a platinum paste (Platinum Paste, Dyesol Ltd) on a FTO/glass substrate, followed by firing at 450 °C for 30 min with a temperature ramp rate of 15 °C min^{-1}. Screen printed silver paste (Dupont) strips were used to make contacts between cells and the external circuit output. The silver paste was fired at 450 °C for 30 min. DSCs were assembled by sealing the CE and the dye-coated PE with a heat treated thermoplastic sealant (40 μm Binel gasket, DuPont) at 1 bar and 150 °C for 30 s. Electrolyte solutions were injected into the cells, *via* a vacuum back filling technique, through a channel previously realized in the sealant gasket. After electrolyte injection, the channel part of the cell was sealed by hot pressing. The realized masterplate configuration contained 5 equal cells with an active area of 3.6 cm^2 (0.9 cm × 4.0 cm). The total area of one cell comprising both the active area and a monitor electrolyte window was (1.0 cm × 4.6 cm) 4.6 cm^2. The additional electrolyte window allowed monitoring of the degradation of the electrolyte and dye desorption separately.

Thermal stress at 85 °C was performed by leaving the investigated devices in an oven under dark conditions.

Current density–voltage (*J–V*) curves were recorded at different stages during stress duration using a solar simulator with halogen lamps providing 1 Sun illumination (100 mW cm^{-2}). The electrical parameters of the solar cell efficiency (η), open circuit voltage (V_{oc}), short circuit current (J_{sc}) and fill factor (FF) were extracted *via* the 1 Sun *J–V* characteristics as a function of time.

Micro-Raman measurements were performed by focusing the laser beam on TiO_2/dye photo electrodes for fresh cells and aged cells. Raman spectra were acquired through a Jobin-Yvon–Horiba micro-Raman system (LabRAM ARAMIS) equipped with an Ar^+ ion laser (514 nm) as the excitation source (100 mW). The Horiba micro-spectrometer is coupled with a confocal microscope that allows control over the depth within the device. The spectrometer was equipped with a diffraction grating of 1800 lines per mm. The laser light reached the sample surface at normal incidence by means of an ultra-long working distance (50×) objective. The laser spot has a power density of 0.25 mW μm^{-2} on the investigated sample (further details about the system in ref. 21).

IS measurements and dark *J–V* measurements were carried out using a potentiostat unit from Autolab. The IS analyzed frequency range was from 20 mHz to 100 kHz. The IS measurements were performed under dark conditions over the voltage range of −0.8 to 0 V in 50–100 mV step intervals. The Z-View software from Scribner Inc. was used for the data fitting.

Results and discussion

The *J–V* curves under 1 Sun illumination are reported in Fig. 1a for fresh Z907/HSE and Z907/L-12 cells, and for fresh Ru505/HSE

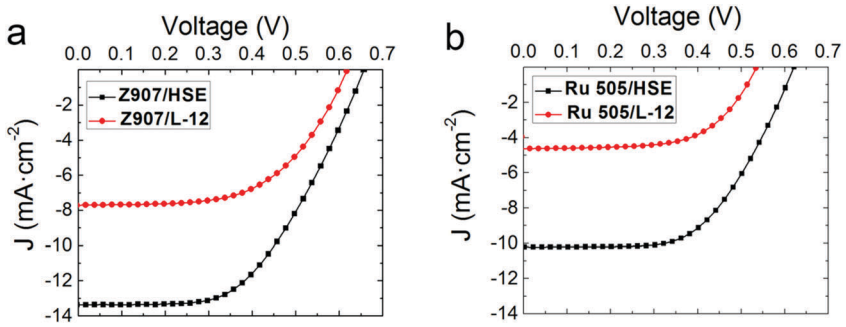

Fig. 1 *J–V* curve at 1 Sun illumination for (a) Z907 and (b) Ru505 cells.

and Ru505/L-12 cells in Fig. 1b. Notably, cells employing Z907 and Ru505 dyes with the HSE electrolyte showed efficiency 1.7 and 2.1 times higher than the same devices employing the L-12 electrolyte.

The higher short circuit current density (J_{sc}) values recorded for devices using the Z907 sensitizer with respect to the Ru505-based devices (see Table 1) are ascribable to the broader absorption spectrum in the spectral region above 550 nm (see ESI,† Fig. S1). On the other hand, owing to the employed electrolyte, higher open circuit voltages (V_{oc}) were recorded in Z907/HSE and Ru505/HSE compared to the Z907/L-12 and Ru505/L-12 devices. The as-prepared devices underwent a prolonged thermal stress at 85 °C in the oven and under dark conditions for 4700 h. Fig. 2 summarizes the electrical parameter evolution (J_{sc}, V_{oc}, fill factor and efficiency) during the stress time for each tested cell. It is seen that the Z907/HSE, Z907/L-12, Ru505/HSE and Ru505/L-12 devices retain 30%, 60%, 65% and 95% of their initial efficiencies, respectively. Considerably, the devices based on the L-12 electrolyte showed a slower degradation rate with respect to the HSE-based devices. In particular, the Ru505/L-12 cell showed the slowest efficiency degradation rate (1% per 1000 h) reflecting in 4%, 3% and 7% loss in efficiency, J_{sc} and V_{oc}, respectively.

Several degradation mechanisms were observed during the thermal aging for the different electrolytes. In the case of the HSE-based devices, the most relevant performance reduction has been associated with the electrolyte leakage occurring after ~3100 h of thermal stress, while the devices remained relatively undamaged when the L-12 electrolyte is employed. This is reflected in the fact that in the case of HSE-based cells, the aging produced large current losses reflecting in 50% and 80% efficiency loss when Ru505 and Z907 sensitizers were used, respectively. C. Han and S. Park[22] observed that the stress induced by the electrolyte expansion could break the encapsulation and could permit the electrolyte leakage with the formation of island-type defects. A similar phenomenon has been observed in the case of the HSE-based devices (see Fig. 9c). This can be definitively explained by the degradation and/or the thermal expansion of the MPN solvent within the HSE causing electrolyte leakage under prolonged heating conditions. Thus, in the case of a nitrile-based solvent with a low boiling point, glass-frit encapsulation represents a valid alternative to the thermoplastic sealant in order to make the DSC system more robust.[23] On the other hand, by analyzing the comparison between devices differing only in the sensitizer employed, as reported in Fig. S2a and b (ESI†), it is noteworthy that Ru505-based devices limit the performance losses, without noticeable changes for the first 3100 h, see Fig. 2(b), independently from the employed electrolyte.

Table 1 Electrical parameters for the investigated fresh cells extracted by the 1 Sun *J–V* curves

Cells/parameters	V_{oc} (mV)	J_{sc} (mA cm^{-2})	Fill factor (%)	Efficiency (%)
Z907/HSE	663	13.09	56.2	4.87
Z907/L12	610	7.91	57.5	2.78
Ru505/HSE	656	10.46	60.3	4.35
Ru505/L12	585	6.30	61.8	2.22

For further insight into the degradation mechanisms, the absorption spectra of the Z907-based devices are reported in Fig. 3 for both the HSE (Fig. 3a) and L-12 (Fig. 3b) electrolytes in the cases of fresh (black curves) devices and after 1000 h of temperature stress (red curves).

After a 1000 h aging test, we could not observe electrolyte leakage from the active area even if a slight decrease in the absorbance spectrum (Fig. 3a and b) in the low wavelength region ($\lambda < 480$ nm) can be noted. This effect has been associated with a decrease of free triiodide species within the electrolyte solution, as confirmed by Raman analysis reported in the following section. Moreover, the recorded decrease of dye absorbance for the Z907/HSE device reflects the degradation of the Z907 dye molecules due to the interaction between the MPN solvent and the PE,[23] which was not observed in the case of Ru505-based devices. Moreover, incident photon to current conversion efficiency (IPCE) spectra for the L-12-based devices (Fig. 3d) do not show an appreciable decrease after 1000 h of thermal stress, confirming the improved stability of the TiO_2/dye/electrolyte interface for the L-12 cells with respect to HSE-based systems (Fig. 3c). As a matter of fact, the degradation of the electrolyte was found to be thermally activated, resulting in the growth of a uniform solid electrolyte interphase (SEI) layer that wraps TiO_2 in the case of the MPN-based (HSE) electrolyte.[24] The SEI growth stems from the degradation of the solvent and electrolyte additives and even includes trapped triiodide/iodide ions. This phenomenon leads to triiodide depletion in the electrolyte, causing the downshift in intra-band trap

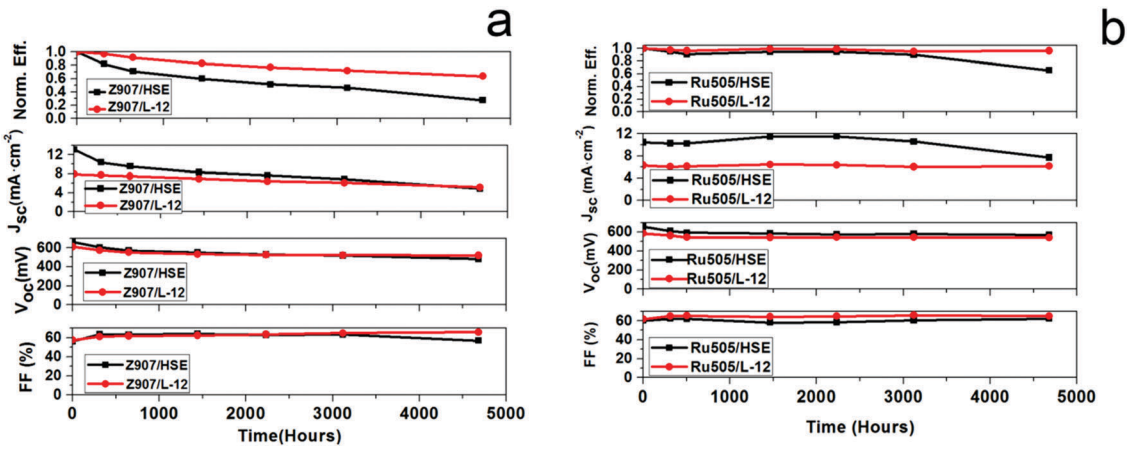

Fig. 2 The electrical parameters for (a) Z907/HSE and Z907/L-12 (b) Ru505/HSE and Ru505/L-12 under temperature stress at 85 °C as a function of time under 1 Sun AM 1.5G 1000 W m^{-2}.

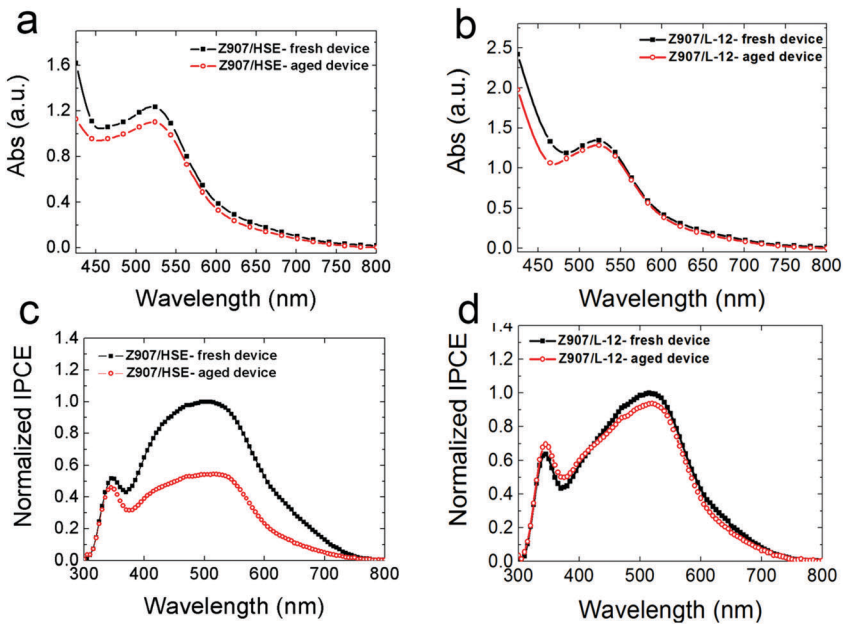

Fig. 3 Absorption (panels a and b) and IPCE (panels b and c) spectra for Z907/HSE (panels a and c) and Z907/L-12 (panels b and d) devices acquired on fresh cells (black curves) and after 1000 h of thermal stress at 85 °C (red curves).

states in TiO_2 and the modification in the cell charge dynamic, as will be confirmed in this work by IS analysis. In contrast, the absence of the nitrile-based solvent has been already demonstrated to drastically improve the DSC stability under prolonged thermal stress[15] by preventing the TiO_2/dye/electrolyte interface degradation, as confirmed in the case of L12-based devices from IPCE spectra (Fig. 3d).

With the aim to deeply investigate the electrolyte influence on the stability of the device, we performed IS analysis on both fresh and aged tested devices. The Nyquist plots are reported in Fig. 4 for both fresh Z907 (Fig. 4a) and Ru505 (Fig. 4b) based solar cells.

The typical Nyquist plot for a DSC exhibits three semicircles from low to high frequencies (from right to left on the *x*-axis of Fig. 4). From the first arc at high frequency, it is possible to extract the CE charge transfer resistance R_{Pt}, from the second one the recombination resistance at the TiO_2/electrolyte interface R_{rec} and finally from the low-frequency arc the electrolyte diffusion resistance R_d. In fact, the width of each arc corresponds to R_{Pt}, R_{rec} and R_d, respectively, while the initial displacement of the arcs from the origin corresponds to the contribution from the FTO resistance R_s,[25,26] mainly arising from the FTO contacts. We use the circuit shown in Fig. 5 for the Nyquist plot fitting, where L is the inductive element due to wires connecting the cell to the measurement instrument, which corresponds to the delay of the current with respect to fast voltage variations (see Fig. S3, ESI†), C_{pt} is the capacitance at the Pt electrode, C_μ (= $c_\mu \cdot L_f$, where L_f is the thickness of the

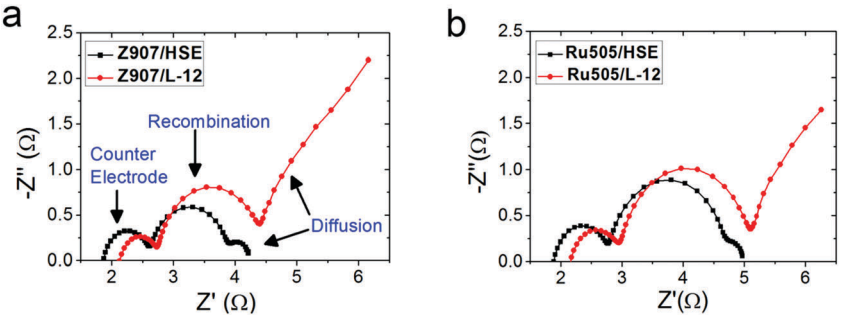

Fig. 4 Nyquist plots at V = 0.8 V, recorded in the dark for (a) Z907 and (b) Ru505 cells.

TiO_2 film) is the chemical capacitance of TiO_2.[25,27–29] R_{series} is the total series resistance given by

$$R_{series} = R_s + R_d + R_{Pt} \quad (1)$$

From these values, the total potential drop through the cell can be estimated to finally extract the potential at the semiconductor, V_F. Finally, the electron diffusion length L_n can be calculated as $L_n = L_f(R_{rec}/R_{tr})$,[1/2] where $R_{tr}(= r_{tr}\cdot L_f)$ is the transport resistance at the corresponding applied potential.[30] The comparison between the HSE and L-12 Nyquist plots reported in Fig. 4a shows for the L12 electrolyte that (i) the larger R_d (larger arc at low frequency) and (ii) the arcs shift towards higher real part values due to an increased device series resistance, R_s. The one order of magnitude larger R_d value found for the L12 electrolyte with respect to the HSE electrolyte was associated to the higher viscosity of L12 compared to HSE,[31] which is responsible for mass transport limitations of iodide ions as described by[13,32,33]

$$K_{et} \propto \vartheta^{-1} \quad (2)$$

where K_{et} is the charge transport rate constant in the electrolyte and ϑ its viscosity.

The electrolyte impacts on both the R_d, taking into account the ion concentration gradient in the solution, and R_s values, considering the bulk ion concentration.[24,33] The observed higher R_s, in the case of the L-12 based device, can be ascribed to the higher L-12 viscosity, since R_s has contributions from the TCO, wires and electrolyte bulk resistances. In the same way, the large R_d value due to L-12 diffusion limitation slows down the dye regeneration rate, explaining the reduced J_{sc} in L-12 samples. In contrast, impedance spectra reported in Fig. 4a showed only small changes in recombination at the TiO_2/dye/electrolyte interface and in charge transfer at the Pt/electrolyte CE when passing from the HSE to the L-12 electrolyte.

In order to clarify the degradation mechanisms, IS data were acquired for strongly degraded DSCs employing Z907 (Fig. 6) and Ru505 sensitizers (Fig. S5, ESI†). At lower absolute values of applied voltages, the Fermi level is not high enough to inject electrons into the conduction band of TiO_2, leading to very high R_{tr} values, as shown in Fig. 6c. Hence, at these potentials, we observe charging of the FTO/electrolyte interface (Fig. 6a). At moderate negative potentials, the injection of electrons into the conduction band occurs by increasing the conductivity of TiO_2 and eventually reducing the R_{tr} value. By increasing the V_F absolute value above −0.5 V, we observed a sharp increase in the bulk capacitance $C_{TiO_2/FTO}$, which is associated with the chemical capacitance of TiO_2. From Fig. 6a and c, it appears that no significant change in the position of the conduction band occurred despite a change in the slope of $C_{TiO_2/FTO}$ and R_{tr} for the Z907/HSE samples after aging. This behavior can be ascribed to a change in the density of TiO_2 mid-gap states. The aged Z907/HSE cell also showed one order of magnitude reduction in R_{rec} at more negative potentials compared to the fresh Z907/HSE cell. This reflected directly in the shift of the

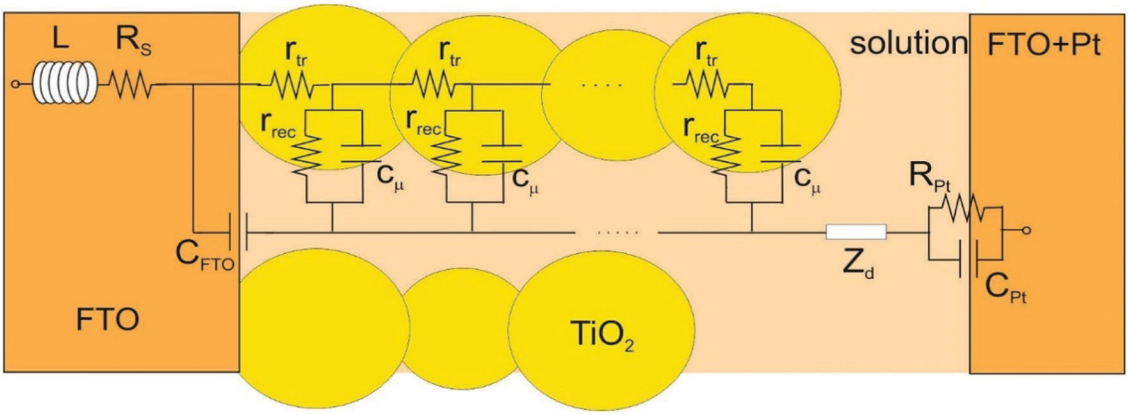

Fig. 5 The transmission line model for impedance data fitting.

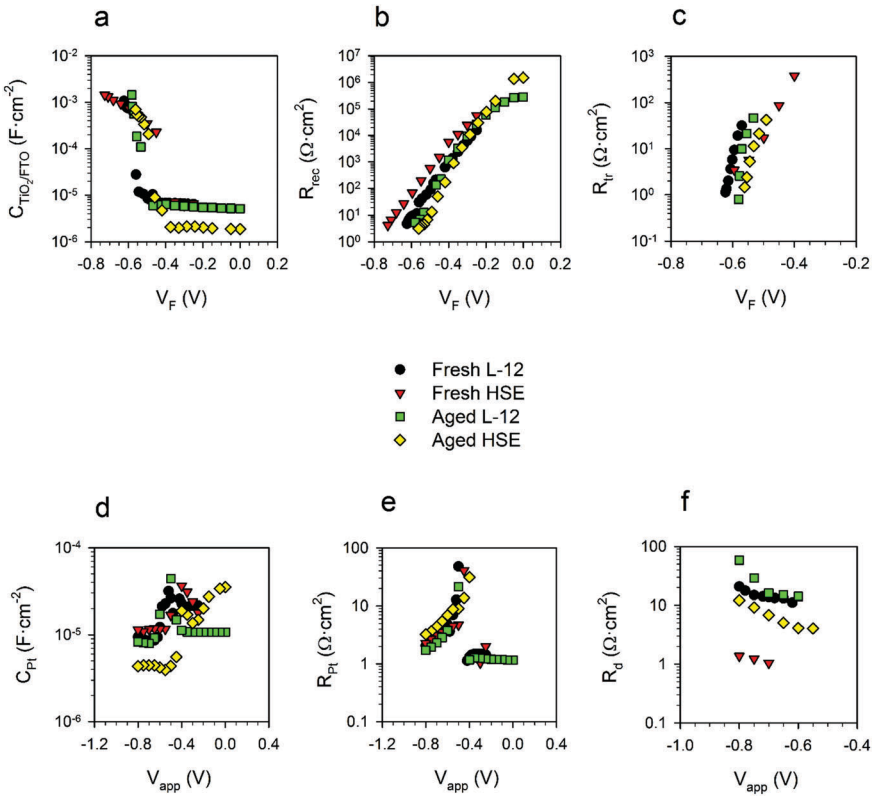

Fig. 6 Evolution of (a) bulk capacitance, (b) recombination resistance R_{rec} of TiO_2 electrode, (c) electron transport resistance in the conduction band of TiO_2 with respect to the potential at the semiconductor V_F and evolution of (d) platinum CE capacitance, (e) CE charge transfer resistance and (f) electrolyte ion diffusion resistance by varying the applied voltage, for both fresh and aged cells fabricated with the Z907 sensitizer.

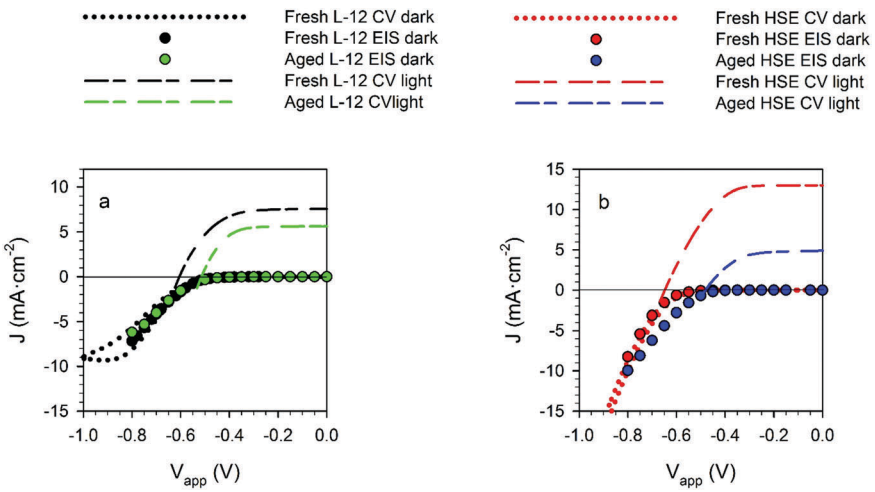

Fig. 7 *J–V* curves obtained from IS and cyclic voltammetry (CV) measurements for (a) Z907/L-12 cells (b) Z907/HSE cells.

exponential recombination current density onset in the *J–V* curve (Fig. 7) for aged Z907/HSE cells compared to fresh Z907/HSE cells. This can be related to the increased recombination kinetics after the formation of the oxidized dye–triiodide $[D^+I_3^-]$ complex in the aged Z907/HSE cells, which has been detected by Raman spectroscopy, described in the subsequent sections.

We also note that the capacitance of the Pt/electrolyte interface C_{Pt} (Fig. 6d) and the FTO/electrolyte interface (Fig. 6a) in the case of the degraded HSE sample has been reduced by a half order of magnitude. This may be related to the electrolyte leakage, which reduces the contact area between the Pt electrode and the FTO with the electrolyte solution.

Moreover, from the shift observed in R_{rec} values of Fig. 6b, a significant reduction in V_{oc} of about 160 mV in Z907/HSE cells can be expected for the aged Z907/HSE samples. In fact, the V_{oc} decrease may occur due to a shift in the electron conduction

band or changes in the recombination kinetics.[27] Since the band (or capacitance) shift reported in Fig. 6a is small (even considering electrolyte leakage) for the HSE samples, we can associate the loss in potential occurring in the aged Z907/HSE sample to mainly a large increase in the recombination kinetics. On the other hand, in the case of the Z907/L-12 samples, carrier recombination losses appear to have been only slightly accelerated by the aging process, as confirmed by the overlapping of R_{rec} values extracted for the fresh and aged samples (Fig. 6b). The small R_{rec} decrease recorded in the case of the Z907/L-12 aged sample for more negative potentials is in good agreement with the $\sim$50 mV shift towards lower potentials showed in both R_{tr} (Fig. 6c) and $C_{TiO_2/FTO}$ (Fig. 6a) *vs.* V_F plots. This shift is indicative of an electron conduction band shift to lower energies occurring after the thermal aging. Hence, the recombination kinetics are actually the same in the fresh and aged Z907/L-12 cells, as seen from the plot of R_{rec} *versus* the equivalent conduction band; see Fig. S4 (ESI†). Therefore, from these data, for the aged Z907/L-12 samples, a slight decrease occurred in V_{oc}, around 50 mV, as expected. From the *J–V* curves under illumination shown in Fig. 7, we observed a reduction in V_{oc} of about 160 mV for the aged Z907/HSE samples compared to the fresh ones, which matches the V_{oc} shift predicted from IS measurements (Fig. 6b). We also observed a huge decrease in J_{sc} by 8.1 mA cm^{-2} (Fig. 7), which can be ascribed to the electrolyte leakage even responsible for the large increase of R_d and eventually for the transport limitations in the aged HSE samples, as shown in Fig. 8. On the other hand, the L-12 based fresh cells showed a much larger R_d value (Fig. 6f) than the HSE ones, due to the higher viscosity of the L-12 electrolyte compared to the HSE one. Consequently, the maximum attainable current by the L-12 cell is strongly reduced with respect to the case of HSE-based devices, due to the diffusion constraints (see Fig. 8).

This implies that the spacer between the TiO_2 film and CE should be reduced to a minimum value to maximize J_{sc} in L-12 samples. In L-12 aged samples, the decreased limiting current together with the increased R_d value led to an even stronger limitation in dye regeneration and eventually to a lower J_{sc} value. This result suggests I_3^- and/or iodide depletion upon aging. Notably, the *J–V* curves (Fig. 7) recorded for aged cells both in the dark and under illumination showed increased series resistances (related to the *J–V* curve slope at V_{oc}) that can be related to an increased electrolyte $R_d$value. In addition, the *J–V* curve under illumination for aged Z907/L-12 cells showed a *V*oc decrease of 70 mV with respect to the fresh one (Fig. 7a), slightly higher than the predicted value from IS measurements in the dark. This difference may be related to the decrease (1.95 mA cm^{-}2) in J_{sc} observed for the aged sample or to an increase in the recombination kinetics under illumination with aging. A milder V_{oc} decreasing trend has been observed for the aged Ru505-based devices under prolonged thermal stress (Fig. 2b) that could be ascribed to a TiO_2 surface modification, as suggested by IS analysis reported in the ESI† (Fig. S5).

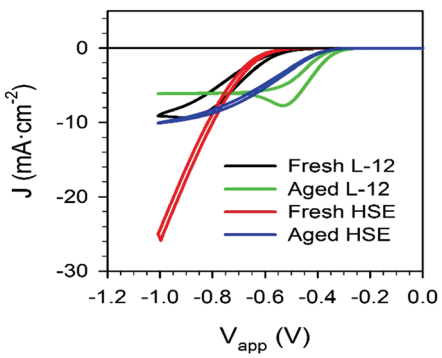

Fig. 8 Dark *J–V* curves of fresh and aged L12 and HSE cells, indicating the diffusion limitations to the current for fresh and aged cells.

Besides the breaking of the encapsulation induced by the thermal expansion of the electrolyte, several intrinsic factors lead to a steady degradation of DSCs especially evident for the Z907 based cells (Fig. 9c). These factors are systematically investigated by means of Raman spectroscopy. Low-frequency region micro-Raman spectra of the fresh and aged devices are reported in Fig. 9a, while the complete Raman spectra related to fresh Z907 and Ru505 based photoelectrodes have been extensively discussed in the literature.[12,34,35] In particular, all the reported Raman spectra exhibit the characteristic Raman-active phonon modes of the tetragonal structure of anatase TiO_2 at 145 cm^{-1} [36,37] that will be employed as a reference peak for the following description, since the TiO_2 mesoporous layer is known to be unaffected by prolonged thermal stress.[38] In all devices, an important interaction between the excited dye (D^+) and tri-iodide (I_3^-) ions has been detected in the micro-Raman spectra at 169 cm^{-1} assigned to the I_3^- symmetric vibration in the [D^+–I_3^-] complex.

The Raman band of the [$D^+I_3^-$] complex at 169 cm^{-1} probed *via* the photo electrode side were found to be highly sensitive to the electrolyte composition variations induced by thermal stress.[6] To quantify this variation, the intensity ratio of the 169 cm^{-1} band relative to the most intense TiO_2 band at 145 cm^{-1} (I_{169}/I_{145}) is extracted by the Raman spectra for each investigated device and reported in Fig. 9b with respect to the J_{sc} values recorded under 1 Sun illumination. In fact, a clear correlation between the electrical cell parameters and the relative intensity of the 169 cm^{-1} mode was already evidenced by Kontos and coworkers,[6] reflecting the depletion of bound triiodides at the dye/TiO_2 interface. A dramatic decline in the intensity ratio was found for the thermal-stressed cells Z907/HSE and Ru505/HSE by $\sim$32% and $\sim$40%, respectively, which is consistent with the strong J_{sc} decrease reported in Fig. 9b for both Z907/HSE and Ru505/HSE devices. The images of the fresh and aged cells of Z907/HSE and Ru505/HSE respectively are shown in Fig. 9c. The above-mentioned reduction of the I_{169}/I_{145} ratio can be ascribed to the triiodide loss at the PE due to the breaking of the sealing in the HSE and the following electrolyte leakage mentioned previously after prolonged annealing. Consequently, the aged devices showed a dramatic reduction in efficiency independently from the employed dye (70% for Z907/HSE and 40% for Ru505/HSE). In contrast, the thermal-stressed Ru505/L-12 based devices showed a moderate decline in the I_{169}/I_{145} ratio (−13.3%) with respect to their corresponding fresh samples,

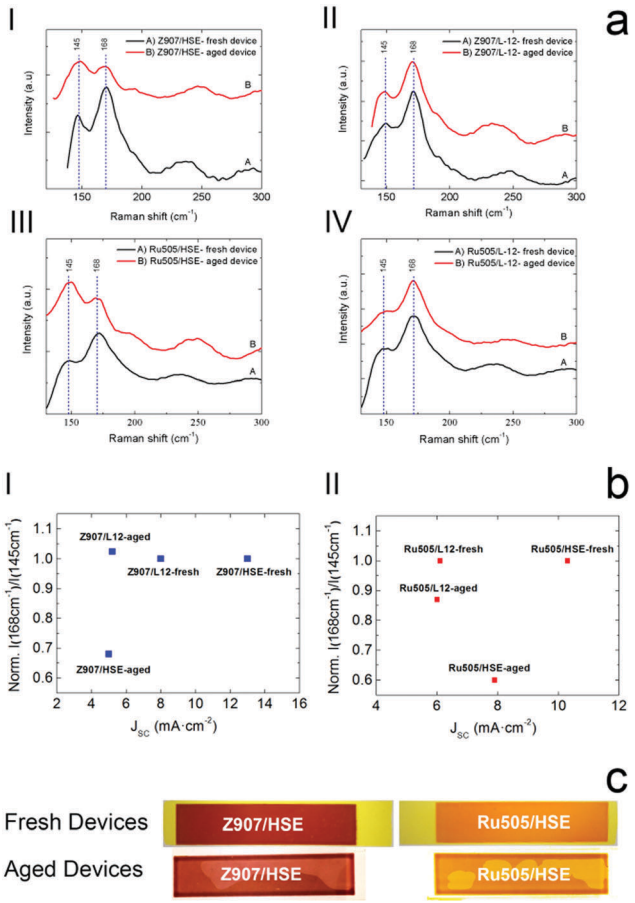

Fig. 9 (a) Low-frequency region of the Raman spectra acquired by focusing the laser beam (514 nm) onto the device's photo-electrode for fresh and thermal stressed cells (4700 h at 85 °C). In particular, the different panels refer to (I) Z907/HSE, (II) Z907/L-12, (III) Ru505/HSE, and (IV) Ru505/L-12. (b) Intensity ratio for (I_{169}/I_{145}) bands of all cells, collected from fresh and aged spectra of all the tested device typologies and after normalizing these values by the numbers for corresponding fresh cells. (c) Images of Z907/HSE and Ru505/HSE, fresh and aged DSCs after thermal stress at 85 °C.

while Z907/L12 exhibited a slight increase (+2.5%) in the considered peak intensity ratio.

In this last case, the $[D^+I_3^-]$ complex increase can be imputed to the partial loss of coordinated SCN^- ligands from the dye molecules,[35] which retains the dye in a prolonged oxidized state. These changes at the TiO_2 surface may be responsible for the small conduction band shift observed from the IS data for Z907/L-12 aged devices. In this context, the coordination between the D^+ and triiodide ions is favored and the formation of Ru(III) intermediates finally leading to Ru(II)(CN), which becomes a possible degradation-induced sub-product.[12,39,40] The interaction between the dye and electrolyte accelerates the recombination kinetics for the aged Z907/HSE devices as also seen from IS, which reflected in a progressive photovoltaic performance reduction for the HSE samples,[41] as shown in Fig. S2a (ESI†). Since the Raman spectrum of the electrolyte acquired on the electrolyte monitor window of the thermal-stressed Z907/L-12 sample reported in our previous publication[34] did not show any Raman features of dye molecules, it is possible to assert that the dye is still anchored on the TiO_2 surface after thermal stress by excluding desorption phenomena. Notably, the absence of any relevant and evident modification in the low-frequency Raman spectrum of Ru505/L-12 devices reported in Fig. 9a panel IV, confirms the chemical stability of the device's constituents and it supports the stable efficiency trend of Fig. 2b under prolonged thermal stress. In fact, devices employing the Ru505 dye showed an improved stability under thermal stress conditions due to the stronger coordination to the ruthenium of CN^- with respect to the SCN^- ligand.[6,12] Thus, the use of a Ru-based dye with cyanide group as ancillary ligands coupled with a more viscous electrolyte (such as L-12 tested in this work) can effectively prevent dye/electrolyte interface degradation under prolonged annealing conditions (85 °C).

Conclusion

Among the different tested dye–electrolyte couples (Z907/HSE, Z907/L-12, Ru505/HSE and Ru505/L-12) for DSCs, the Ru505/L-12 cell demonstrated remarkable stability under prolonged 85 °C thermal stress, with a lifetime of over 4700 h. In particular, devices using the HSE electrolyte suffered harsh J_{sc} and efficiency decrease due to the TiO_2/dye/electrolyte interface degradation coupled to electrolyte leakage. On the other hand, the L-12 devices undergo only moderate electrolyte degradation due to a partial loss of triiodide ions induced by prolonged annealing conditions.

IS analysis performed on Z907 cells revealed a significant reduction in V_{oc} for HSE-based cells, mainly attributed to electrolyte leakage, which was prevented in the case of L-12 cells.

On one hand, the present study demonstrates that the use of a solvent free electrolyte such as L-12 in DSCs is a valid alternative to the unstable nitrile-based electrolyte in avoiding electrolyte degradation and eventually device breakdown under prolonged thermal stress. On the other hand, the demonstrated intrinsic chemical stability of the Ru-505 sensitizer has been identified as the key element in preventing thermally activated TiO_2/dye/electrolyte interface degradation and reduced charge kinetics.

Thus, the Ru-505/L-12 device proposed in this work is a winning strategy in preventing thermally induced degradation mechanisms under real working conditions.

Competing financial interest

The authors declare no competing financial interest.

Acknowledgements

The research leading to these results has received funding from the European Union Seventh Framework Program [FP7/2007-2013] under Grant Agreement 316494 ("DESTINY") and Grant Agreement 609788 ("CHEETAH"). S. R. acknowledges Generalitat Valenciana for the grant GRISOLIA/2014/034.

References

1 B. C. O'Regan and M. Grätzel, *Nature*, 1991, **353**, 737–740.
2 C. R. Osterwald and T. J. McMahon, *Prog. Photovoltaics*, 2009, **17**, 11–33.
3 A. Quatela, A. Agresti, S. Mastroianni, S. Pescetelli, T. M. Brown, A. Reale and A. Di Carlo, *Microelectron. Reliab.*, 2012, **52**, 2487–2489.
4 A. Agresti, L. Cinà, S. Pescetelli, B. Taheri and A. Di Carlo, *Vib. Spectrosc.*, 2016, **84**, 106–117.
5 M. G. Wheatley, A. M. McDonagh, M. P. Brungs, R. P. Chaplin and E. Sizgek, *Sol. Energy Mater. Sol. Cells*, 2003, **76**, 175–181.
6 A. G. Kontos, T. Stergiopoulos, V. Likodimos, D. Milliken, H. Desilvesto, G. Tulloch and P. Falaras, *J. Phys. Chem. C*, 2013, **117**, 8636–8646.
7 M. Toivola, J. Halme, L. Peltokorpi and P. Lund, *Int. J. Photoenergy*, 2009, **2009**, 1–15.
8 L. Ke, S. Bin Dolmanan, L. Shen, P. K. Pallathadk, Z. Zhang, D. Mei, Y. Lai and H. Liu, *Sol. Energy Mater. Sol. Cells*, 2010, **94**, 323–326.
9 N. Kato, Y. Takeda, K. Higuchi, A. Takeichi, E. Sudo and H. Tanaka, *Sol. Energy Mater. Sol. Cells*, 2009, **93**, 893–897.
10 A. Mathew, G. M. Rao and N. Munichandraiah, *Adv. Mater. Lett.*, 2014, **5**, 180–183.
11 E. Figgemeier and A. Hagfeldt, *Int. J. Photoenergy*, 2004, **6**, 127–140.
12 A. Agresti, S. Pescetelli, A. Quatela, S. Mastroianni, T. M. Brown, A. Reale, C. A. Bignozzi, S. Caramori and A. Di Carlo, *RSC Adv.*, 2014, **4**, 12366.
13 M. Gorlov and L. Kloo, *Dalton Trans.*, 2008, 2655–2666.
14 R. Harikisun and H. Desilvestro, *Sol. Energy*, 2011, **85**, 1179–1188.
15 T. Stergiopoulos, A. G. Kontos, N. Jiang, D. Milliken, H. Desilvestro, V. Likodimos and P. Falaras, *Sol. Energy Mater. Sol. Cells*, 2016, **144**, 457–466.
16 N. Jiang, T. Sumitomo, T. Lee, A. Pellaroque, O. Bellon, D. Milliken and H. Desilvestro, *Sol. Energy Mater. Sol. Cells*, 2013, **119**, 36–50.
17 B. E. Hardin, J. Snaith and M. D. Mcgehee, *Nat. Photonics*, 2012, **6**, 162–169.
18 Y. Tachibana, J. E. Moser, M. Gratzel, D. R. Klug, J. R. Durrant, M. Graetzel, D. R. Klug and J. R. Durrant, *J. Phys. Chem.*, 1996, **100**, 20056–20062.
19 S. A. Haque, Y. Tachibana, R. L. Willis, J. E. Moser, M. Grätzel, D. R. Klug and J. R. Durrant, *J. Phys. Chem. B*, 2000, **104**, 538–547.
20 M. Wang, C. Grätzel, S. M. Zakeeruddin and M. Grätzel, *Energy Environ. Sci.*, 2012, **5**, 9394–9405.
21 V. A. Tran, T. T. Truong, T. A. P. Phan, T. N. Nguyen, T. Van Huynh, A. Agresti, S. Pescetelli, T. K. Le, A. Di Carlo, T. Lund, S.-N. Le and P. T. Nguyen, *Appl. Surf. Sci.*, 2017, **399**, 515–522.
22 C. Han and S. I. Park, *15th International Conference on Thermal, Mechanical and Multi-Physics Simulation and Experiments in Microelectronics and Microsystems, EuroSimE* 2014, 2014, pp. 1–5.
23 Y. Jo, J. Y. Cheon, J. Yu, H. Y. Jeong, C.-H. Han, Y. Jun and S. H. Joo, *Chem. Commun.*, 2012, **48**, 8057–8059.
24 C.-Y. Huang, C.-F. You, C.-E. Cheng, B.-C. Lei, J.-C. Jhang, F.-C. Yu, C.-S. Chang and F. S. Sen Chien, *Opt. Mater. Express*, 2016, **6**, 1024.
25 F. Fabregat-Santiago, J. Bisquert, G. Garcia-Belmonte, G. Boschloo and A. Hagfeldt, *Sol. Energy Mater. Sol. Cells*, 2005, **87**, 117–131.
26 E. J. Juarez-Perez, M. Wußler, F. Fabregat-Santiago, K. Lakus-Wollny, E. Mankel, T. Mayer, W. Jaegermann and I. Mora-Sero, *J. Phys. Chem. Lett.*, 2014, **5**, 680–685.
27 H. Greijer Agrell, J. Lindgren and A. Hagfeldt, *J. Photochem. Photobiol., A*, 2004, **164**, 23–27.
28 S. R. Raga, E. M. Barea and F. Fabregat-santiago, *J. Phys. Chem. Lett.*, 2012, **3**, 1629–1634.
29 J. Halme, P. Vahermaa, K. Miettunen and P. Lund, *Adv. Energy Mater.*, 2010, **22**, 210–234.
30 S. Mastroianni, A. Lanuti, S. Penna, A. Reale, T. M. Brown, A. Di Carlo and F. Decker, *ChemPhysChem*, 2012, **13**, 2925–2936.
31 F. Fabregat-Santiago, J. Bisquert, E. Palomares, L. Otero, D. Kuang, S. M. Zakeeruddin and M. Gra, *J. Phys. Chem.*, 2007, **2**, 6550–6560.
32 J. Bisquert, *J. Phys. Chem. B*, 2002, **106**, 325–333.
33 M. Toivola, F. Ahlskog and P. Lund, *Sol. Energy Mater. Sol. Cells*, 2006, **90**, 2881–2893.
34 S. K. Yadav, A. Agresti, S. Pescetelli, L. Cinà, D. Gentilini and A. Di Carlo, *Proceedings of the 15th IEEE International Conference on Nanotechnology July*, Rome, Italy, 2015, pp. 381–384.
35 S. Sarker, H. W. Seo and D. M. Kim, *Chem. Phys. Lett.*, 2013, **585**, 193–197.
36 N. W. Duffy, K. D. Dobson, K. C. Gordon, B. H. Robinson and A. J. Mcquillan, *Chem. Phys. Lett.*, 1997, **266**, 451–455.
37 C. Pérez-Leon, L. Kador, B. Peng and M. Thelakkat, *J. Phys. Chem. B*, 2006, **110**, 8723–8730.
38 V. Likodimos, T. Stergiopoulos, P. Falaras, R. Harikisun, J. Desilvestro and G. Tulloch, *J. Phys. Chem. C*, 2009, **113**, 9412–9422.
39 A. Agresti, S. Pescetelli, E. Gatto, M. Venanzi and A. Di Carlo, *J. Power Sources*, 2015, **287**, 87–95.
40 P. H. Svensson and L. Kloo, *Chem. Rev.*, 2003, **103**, 1649–1684.
41 B. O'Regan, I. Lopez-Duarte, M. V. Martınez-Diaz, A. Fornelli, J. Albero, A. Morandeira, E. Palomares, T. Torres and J. R. Durrant, *J. Am. Chem. Soc.*, 2008, **130**, 2906–2907.

